Third-Generation Cardiovascular Phantom The Next Generation of Preclinical Research in Diagnostic Imaging

Third-Generation Cardiovascular Phantom
The Next Generation of Preclinical Research in Diagnostic Imaging

Michael C. McDermott, BSc,†‡ Thomas Sartoretti, BSc,*†§ Casper Mihl, MD, PhD,*† Hubertus Pietsch, VMD, PhD,‡ Hatem Alkadhi, MD, PhD,§ and Joachim E. Wildberger, MD, PhD*†*

Objective: Different types of preclinical research tools used in the field of diagnostic imaging such as dynamic flow circulation phantoms have built the foundation for optimization and advancement of clinical procedures including new imaging techniques. The objective was to introduce a third-generation phantom, building on the limitations of earlier versions and unlocking new opportunities for preclinical investigation.

Material and Methods: A third-generation phantom was designed and constructed comprising physiological vascular models from head to toe, including a 4-chamber heart with embedded heart valves and a controllable electromechanical pump. The models include modular segments, allowing for interchangeability between healthy and diseased vessels. Clinical sanity checks were performed using the phantom in combination with a dual-head power injector on a third-generation dual-source computed tomography scanner. Contrast media was injected at 1.5 g I/s, and the phantom was configured with a cardiac output of 5.3 L/min. Measurements of mean transit times between key vascular landmarks and peak enhancement values in Hounsfield units (HUs) were measured to compare with expected in vivo results estimated from literature.

Results: Good agreement was obtained between literature reference values from physiology and measured results. Contrast arrival between antecubital vein and right ventricle was measured to be 13.1 ± 0.3 seconds. Transit time from right ventricle to left ventricle was 12.0 ± 0.2 seconds, from left internal carotid artery to left internal jugular vein 7.7 ± 0.4 seconds, and 2.9 ± 0.2 seconds from aortic arch to aortic bifurcation. The peak enhancement measured in the regions of interest was between 336 HU and 557 HU.

Conclusions: The third-generation phantom demonstrated the capability of simulating physiologic in vivo conditions with accurate contrast media transport timing, good repeatability, and expected enhancement profiles. As a nearly complete cardiovascular system including a functioning 4-chamber heart and interchangeable disease states, the third-generation phantom presents new opportunities for the expansion of preclinical research in diagnostic imaging.

Key Words: phantom, preclinical, research, radiology, vascular surgery, circulation, vascular, angiography, contrast media, computed tomography

(*Invest Radiol* 2022;57: 834–840)

The field of computed tomography (CT) has undergone substantial transformation in the last 50 years. This has been driven primarily by technological advancements including most prominently spiral CT, multidetector CT, dual-source and dual-energy CT, as well as more powerful x-ray beams and iterative reconstruction algorithms.[1–5] Recently, artificial intelligence–based image interpretation tools and the clinical introduction of photon-counting detector CT have continued the arc of innovation.[6–9] Each step forward has unlocked new opportunities for optimization of clinical routine, resulting in new indications and improvement in diagnostic image quality while reducing effective radiation exposure and administered iodinated contrast media (CM) volumes.[10,11] Unlike optimization of therapeutic techniques for improving patient outcomes, where the pathway to adoption in the clinic must run through in vivo studies, further ethical challenges are faced in x-ray diagnostic imaging when evaluation comes at the cost of ionizing radiation exposure to the patient.[12]

Although clinical studies with patients remain the criterion standard, researchers have made use of preclinical evaluation tools to understand underlying physiological principles, as well as advancing clinical understanding and knowledge while avoiding unnecessary radiation exposure to patients. These tools include benchtop engineering test setups, computer modeling software, radiation dose phantoms, animal models, and dynamic flow circulation phantoms.[13–18] Over the past 2 decades, the dynamic flow circulation phantoms have been used in evaluation and optimization of contrast-enhanced CT procedures. These circulation phantoms are intended to represent the dynamic blood flow within a human cardiovascular system and provide a stable testing platform allowing for high levels of standardization and reduced variability. One of the earliest circulation phantoms used in combination with CT was introduced by Awai et al[19] in 2006, with the goal of simulating aortic peak enhancement after intravenous administration of iodinated CM. The authors validated the ability of this first-generation phantom to replicate similar timing and aortic enhancement profiles in phantom and human studies.[19] In 2008, Behrendt et al[20] introduced a phantom with separate pulmonary circulation, including discrete physiologic arterial pressures.

This phantom, hereafter referred to as the second-generation design, was optimized with additional arterial vascular regions of interest (ROIs) including coronaries and carotid arteries, a thoracic and abdominal aorta, renal arteries, iliac arteries, and physiologic control over cardiac output and blood pressure.[20] For more than a decade, this second-generation circulation phantom was used for evaluation of new scanner technologies, reconstruction techniques, and understanding of factors affecting the optimization of contrast injection protocols in CT.[21–24] However, there exist several limitations to the second-generation phantom design that restrict the boundaries of its clinical utility. These include the lack of a heart model, the lack of cerebral and peripheral vasculature, venous vasculature composed of simple cylindrical tubing, limited ability to evaluate varying pathologies, and no control over cardiac rhythm and waveforms (eg, atrial fibrillation, ventricular tachycardia, etc) other than simple heart frequency and stroke volume. Further, the flow through the second-generation phantom was retrograde during diastole due to the lack of pressure isolating heart valves, reducing the physiological accuracy.

A new third-generation (hereafter third-gen) phantom design is introduced. The objective was to build on the limitations of the earlier generations, whereas unlocking new opportunities for previously unexplored preclinical investigation. The following provides a thorough overview of the third-gen phantom from head to toe, highlighting the key capabilities and opportunities.

Received for publication March 30, 2022; and accepted for publication, after revision, May 2, 2022.

From the *Department of Radiology and Nuclear Medicine, Maastricht University Medical Center, Maastricht, the Netherlands; †CARIM School for Cardiovascular Diseases, Maastricht University; ‡Bayer AG, Berlin, Germany; and §Institute of Diagnostic and Interventional Radiology, University Hospital Zurich, University of Zurich, Zurich, Switzerland.

Funding for materials and construction of phantom were provided by Bayer AG, Berlin, Germany. Design and manufacturing of the vascular models for the phantom were conducted by partnership with United Biologics Inc, Santa Ana, CA.

Correspondence to: Michael C. McDermott, BSc, Department of Radiology and Nuclear Medicine, Maastricht University Medical Center, P. Debyelaan 25, PO Box 5800, 6202 AZ Maastricht, the Netherlands. E-mail: m.mcdermott@maastrichtuniversity.nl.

Supplemental digital contents are available for this article. Direct URL citations appear in the printed text and are provided in the HTML and PDF versions of this article on the journal's Web site (www.investigativeradiology.com).

ISSN: 0020-9996/22/5712–0834
DOI: 10.1097/RLI.0000000000000894

MATERIALS AND METHODS

Phase I: Design and Construction

The third-gen phantom is a preclinical testing platform consisting of 2 major components: the vascular model and the electromechanical pump. The vascular model includes nearly complete venous and arterial circulation from head to toe with the exclusion of minor vessels and the microenvironment of the capillary networks (Fig. 1). The vascular models are based on real human CT data and manufactured using a proprietary silicone printing technology allowing for complex and accurate vascular lumen geometries (United Biologics Inc, Santa Ana, CA). The mechanical properties of the silicone material used to make the models include an elastic modulus between 3.1 and 3.4 MPa as described by the vendor, which is within the range expected for human vascular tissue under standard hemodynamic conditions (1.2–12.2 MPa).[25] The SuperPump (ViVitro Labs, Victoria, British Columbia, Canada) is an electromechanical pump connected to the vascular model. This pump has been used extensively throughout scientific literature and includes a hydraulically activated piston allowing for digital control over pulsatile, physiological, and pathological cardiac flow conditions.[26–28] The pump allows for adaptation of stroke volume from 0 to 180 mL, heart rate from 3 to 200 beats per minute, blood pressure up to 300 mm Hg at 70 beats per minute, and a sophisticated waveform generator software (ViViTest; ViVitro Labs, Victoria, British Columbia, Canada) allowing for the implementation of custom cardiac waveforms simulating various states of cardiac disease and arrhythmia.

The pump drives the dynamics of the phantom, with pulsatile flow generating motion of the heart model (see Video, Supplemental Digital Content 1, http://links.lww.com/RLI/A718, which demonstrates the cardiac motion of the phantom), pulsation of the arterial vascular models, and activation of the heart valves (see Video, Supplemental Digital Content 2, http://links.lww.com/RLI/A719, which demonstrates the activation and function of the embedded heart valves). A schematic of the connection of the pump to the phantom is shown in Figure 2C. An output of the waveform from the pump can be connected to standard electrocardiogram leads from the scanner allowing for electrocardiogram-gated evaluations. Further, the pump system is capable of capturing inputs from pressure and flow transducers to provide control and oversight of hydrodynamic performance within the phantom model. These pressure and flow transducers were used to validate the experimental setup of the model before use.

Head and Neck

Although the figurative brain of the phantom lies within the complex pump system, the literal brain is represented by key arterial vascular structures including the circle of Willis and all relative communicating cerebral arteries (Figs. 3A, B). This healthy cerebral arterial model can be replaced with a model including aneurysms of varying sizes (Fig. 3C). The venous return for the brain includes a moderately complex sinus network as well as internal jugulars providing necessary vascular length to support realistic temporal recirculation periods (Fig. 3D). The neck region includes a normal left internal carotid artery, a tortuous right internal carotid artery, and common carotids to the pericallosal region, with options for stenotic carotid arteries with soft or densely calcified plaques. The venous return from the internal jugulars continues through the neck region for drainage back into the thoracic cavity.

Thorax and Heart

The thoracic section of the phantom from a cranial-caudal perspective includes takeoffs for the neck and cerebral vascular segment, left and right subclavian arteries and veins, and brachiocephalic artery and vein, into a complex and highly physiologic heart model (Figs. 2A–C). The heart comprises 4 chambers with embedded mitral and tricuspid valves including chordae and papillary muscular models for customized

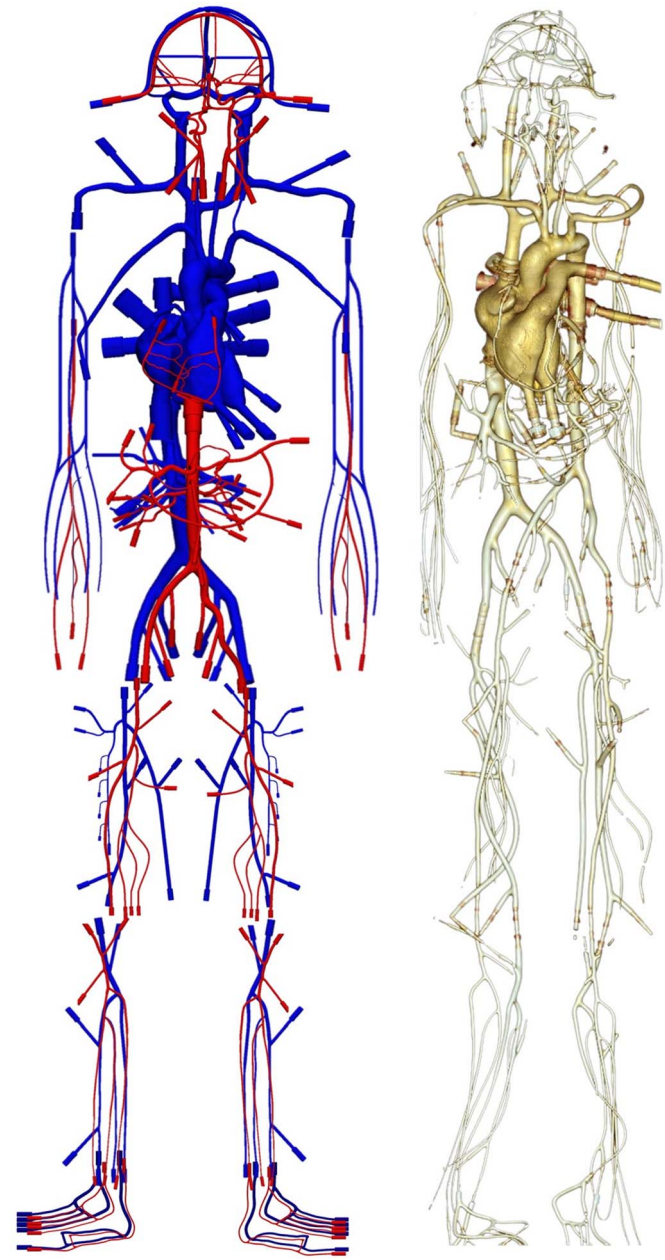

FIGURE 1. Three-dimensional model of the proposed third-gen phantom design (left) and full-body angiogram of the third-gen phantom with volume rendering (right).

control over valve function, as well as embedded aortic and pulmonary valves (Figs. 4A–C). The valves are driven to open and close through pressure differentials created by the pump. A precise coronary ostium allows for modular connection to anatomically accurate left and right coronary branching structures, ending in a common coronary sinus that empties directly into the right atrium. The left and right coronary models allow for stents to be deployed and are replaceable with stenotic versions including soft or densely calcified plaques with varying occlusion percentages (Figs. 5A, B). In addition to an ascending and descending thoracic aorta, simple pulmonary arteries and an inferior pulmonary vein are included. These represent the inlet and outlet points for connection to the pump, which drives physiological flow and facilitates cardiac motion of the model. The complex pulmonary vasculature seen in vivo is replaced

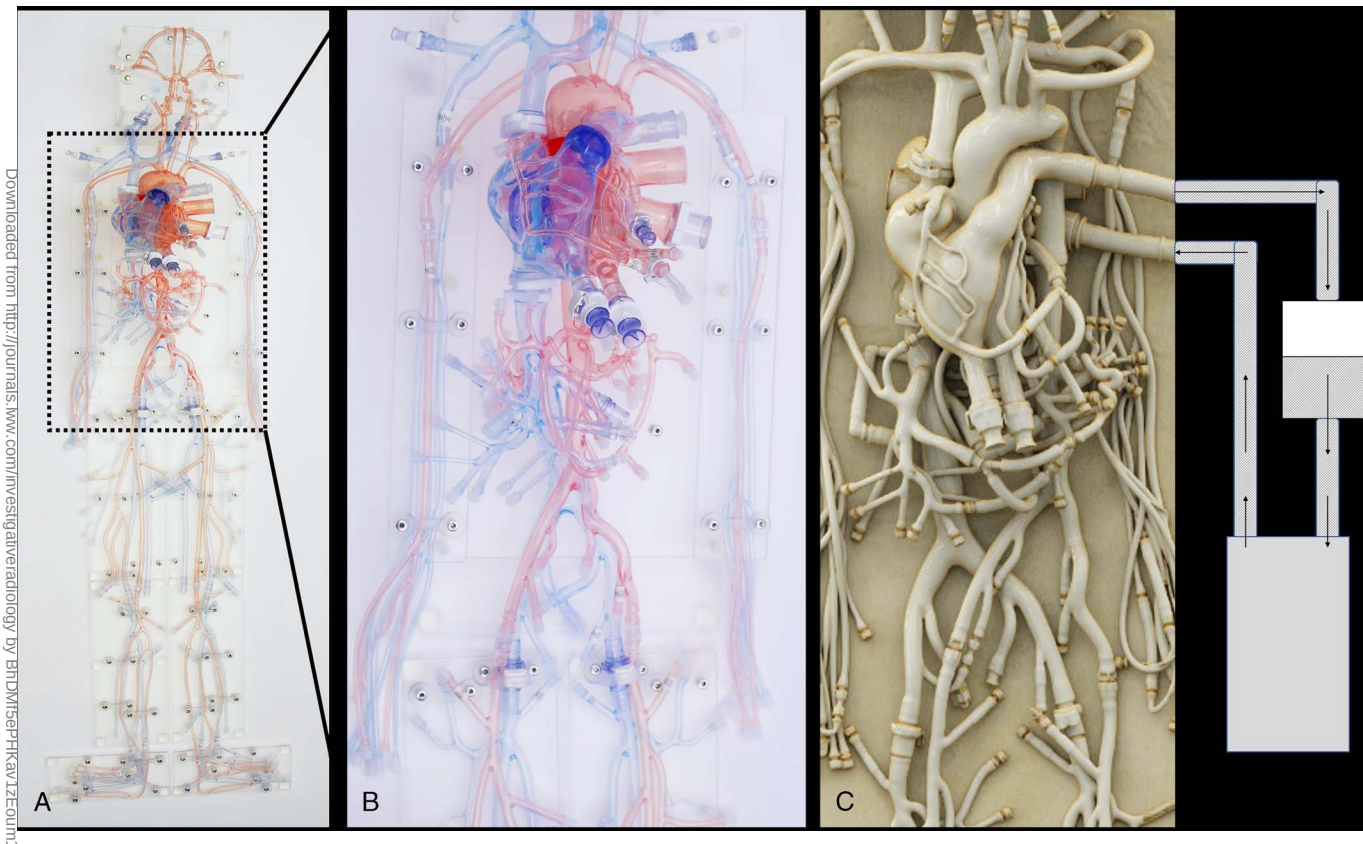

FIGURE 2. A, Image of full body phantom, (B) including zoomed in photograph, (C) 3-dimensional volume rendering of CT angiography data of the thoracic, heart, and abdominal sections, including connection point schematic to pump. Images A and B courtesy of United Biologics Inc, Santa Ana, CA.

on this phantom with a partially air-filled compliance chamber allowing for dynamic control over the compliance effect of the lung compartment on CM transport and distribution dynamics. Similar to the second-generation phantom design, the chamber acts as a capacitor to dampen the flow of CM through the circuit, and the dampening effect is controlled directly by the volume of air filled into the chamber.

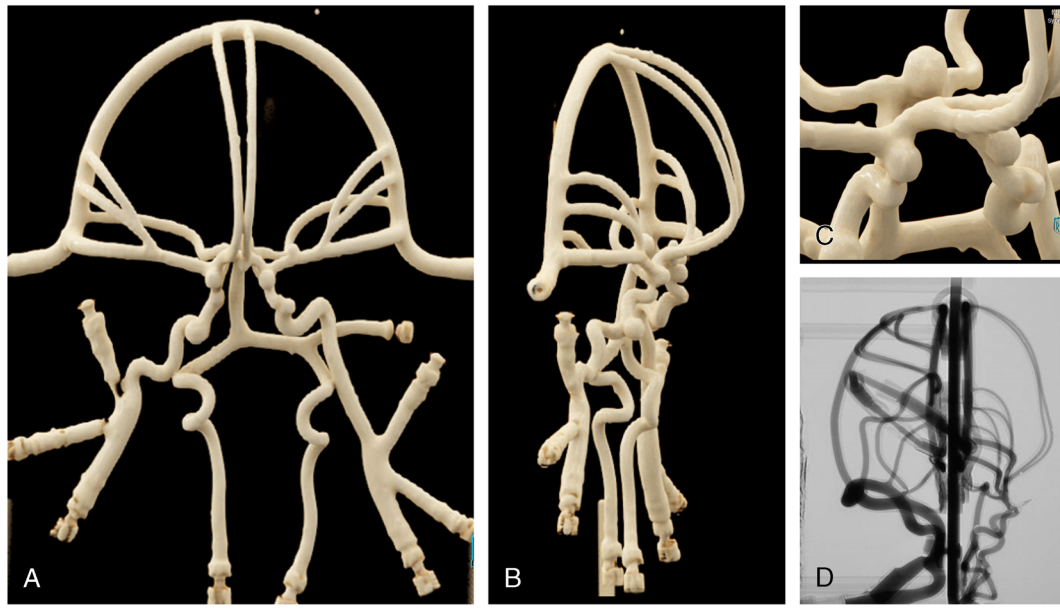

FIGURE 3. A and B, Cerebral arterial vasculature depicted in volume renderings from computed tomography (CT) angiography, (C) volume rendering of actual cerebral aneurysm phantom model from CT angiography, and (D) sagittal fluoroscopy image of cerebral vasculature of the phantom showing venous drainage.

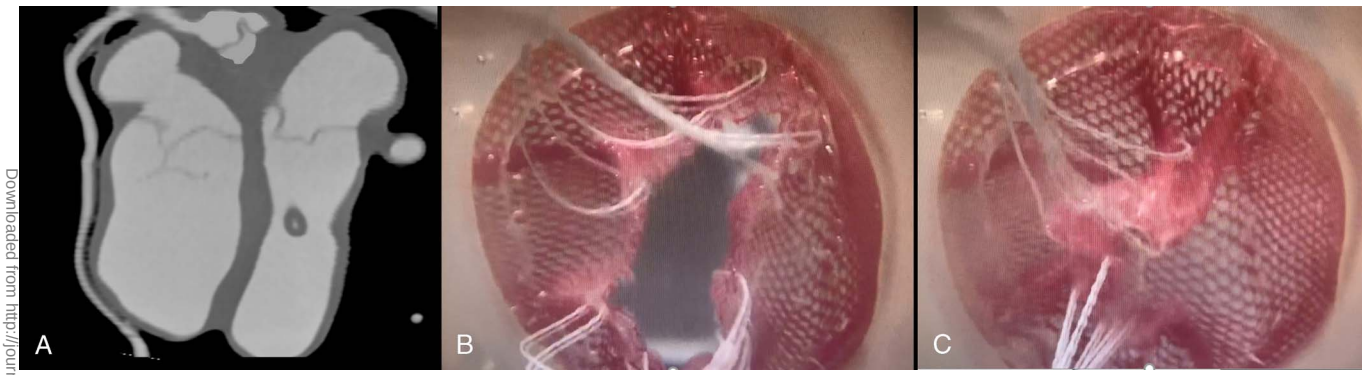

FIGURE 4. Views of the heart of the phantom including (A) coronal reformation demonstrating the right coronary artery with visualization of the 4 heart chambers, valves, and coronary ostium, (B and C) images of one of the functioning embedded valves of the heart in the open (B) and closed position (C). Images B and C courtesy of United Biologics Inc, Santa Ana, CA.

Abdomen

The thoracic aorta descends downward into the abdominal compartment of the phantom, from the abdominal aorta through the iliac bifurcation including internal and external iliac arteries through to the femoral arteries. The abdominal aortic model is capable of being interchanged with a model simulating an abdominal aortic aneurysm.

A complex gastric region is included, along with a tortuous splenic artery, left and right renal arteries, superior and inferior mesenteric arteries, and a common hepatic artery off the celiac trunk. The venous return includes the external iliac veins up through the inferior vena cava, with merging from the superior mesenteric vein, splenic vein, and portal vein.

Peripheral Vessels

The peripheral vasculature of the phantom comprises both arm and leg segments. The arm segments include brachial, radial, ulnar, and common interosseous arteries and veins. The upper leg segment includes common to superficial and deep femoral arteries, with a venous return through the common femoral vein to perforating branches and great saphenous vein. The lower leg is inclusive of popliteal arteries as well as anterior and posterior tibial arteries, with a venous return through the proximal popliteal vein to the peroneal, anterior tibial, and posterior tibial veins. The vascular model comprises left and right foot models stemming from the anterior tibial artery through the dorsalis pedis artery to the medial and lateral tarsal arteries. A dorsal venous return is included.

Phase II: Clinical Sanity Check

To ensure the appropriate CM transport and distribution dynamics throughout the phantom cardiovascular circuit, a sanity check was conducted by measuring 2 of the key metrics that validate accurate correlation of the internal hydrodynamic flow to in vivo conditions. These 2 metrics are (1) the mean transit time (MTT) of the CM, defined as the difference between the time points of peak enhancement between 2 vascular landmarks, and (2) the measured peak enhancement in Hounsfield units (HUs) of the diluted contrast mixture at the ROI. To evaluate MTT, the peaks were fit using open-source fitting software (LabPlot 2.8.2; KDE e.V., Berlin, Germany) to improve temporal resolution. Four specific measurement regions were selected for this sanity check to assess (1) initial contrast arrival time from injection site in the peripheral veins to the right ventricle, (2) mean pulmonary transit time from right ventricle to left ventricle, (3) cerebral transit time from the takeoff of the internal carotid artery to the internal jugular vein, and (4) the aortic flow from the ascending aorta to the iliac bifurcation.

Injection Protocol

A commercially available injection system was used (MEDRAD Centargo; Bayer AG, Berlin, Germany) in combination with a nonionic monomeric iodinated CM agent (iopromide, Ultravist 300; Bayer AG, Berlin, Germany). A typical iodine delivery rate (IDR) of 1.5 g I/s was used, consistent with the range of IDRs used in CT angiography.[29–31] A CM dose volume of 60 mL was selected to produce an injection duration of 12 seconds and was delivered at room temperature.[32] The system was connected to a 20-gauge IV catheter (Becton Dickinson, Franklin Lakes, NJ) inserted into the right antecubital vein of the phantom.

Circulation Phantom

The third-gen phantom was filled with approximately 5.5 L of standard room temperature tap water, and the pump was operated with a cardiac output of 5.3 L/min (70 beats per minute and 75 mL stroke volume) and an internal pressure of 120/80 mm Hg, as measured with a calibrated hemodynamic pressure transducer. The pump was configured with a waveform output simulating normal sinus rhythm. The phantom was drained and flushed twice between each injection to ensure no residual effect of CM recirculation from previous trials. The phantom was surrounded by attenuating structures including tissue-simulating

FIGURE 5. A, Image of active stent deployment in a left coronary vessel, (B) volume rendering of the heart with visualization of coronary stents, (C) image of deposited calcifications in the left internal carotid artery.

TABLE 1. Clinical Sanity Check Results Including MTTs for CM Transport Between Key Arterial Vascular Landmarks Estimated From Literature Versus Third-Gen Phantom, and Peak Enhancement in the Phantom

	Starting Location ROI	Ending Location ROI	MTT (Literature)	MTT (Phantom; n = 3)	Efferent Vessel Peak HU (Phantom)	Afferent Vessel Peak HU (Phantom)
1	Antecubital vein	Right ventricle	10–16 s	13.1 ± 0.3 s	*	557 ± 16 HU
2	Right ventricle	Left ventricle	8–12 s	12.0 ± 0.2 s	557 ± 16 HU	473 ± 12 HU
3	Left ICA	Left IJV	7–10 s	7.7 ± 0.4 s	425 ± 9 HU	*
4	Ascending aorta	Aortic bifurcation	2.4–4 s	2.9 ± 0.2 s	440 ± 7 HU	336 ± 12 HU

*Only arterial vessels measured.

CM, contrast media; third-gen, third-generation; ROI, region of interest; MTT, mean transit time; HU, Hounsfield unit.

attenuation rings. The phantom can also be submerged in water; however, this was not done in this assessment as table motion from shuttle mode may cause motion artifacts due to water displacement.

Computed Tomography Scanner Settings and Image Evaluation

Computed tomography acquisitions for the clinical sanity check were performed on a third-gen dual-source CT scanner (SOMATOM Force; Siemens Healthineers, Forchheim, Germany). Scans were acquired in 4-dimensional with 20 consecutive helical angiograms obtained in shuttle mode (scan length, 454 mm in the *z* axis). The acquisition parameters were as follows: 120 kV, 80 mAs_{Eff}, rotation time of 0.25 seconds, and collimation of 48 × 1.2 mm. Data acquisition was started with a 2-second delay after injection start, with a 2.5-second mean temporal resolution (the relative time difference within 1 shuttle acquisition to return from the middle point-to-point, 20 × 2.5 seconds results in 50 seconds scan duration in total). Images were reconstructed with a slice thickness of 5.0 mm, increment of 3.0 mm, and using a soft tissue convolution kernel (Br36). The peak signal enhancement was derived from the resulting time-enhancement curves using image evaluation software (SyngoVia; Siemens Healthineers, Forchheim, Germany) drawn in the corresponding ROIs as provided in Table 1. The entire injection and scan acquisition were repeated 3 times for all measurement regions to assess variability of the phantom operation, defined as the range in MTTs between the 4 measurement locations. Based on these measurements, mean and standard deviation of the transport time and peak enhancement were calculated.

RESULTS

Good agreement was obtained between physiological literature reference values and measured results. Contrast arrival between antecubital vein and right ventricle was 13.1 ± 0.3 seconds. Transit times from right ventricle to left ventricle were 12.0 ± 0.2 seconds. From left ICA to left IJV, 7.7 ± 0.4 seconds was measured. Finally, 2.9 ± 0.2 seconds was measured from aortic arch to aortic bifurcation. The repeatability (measured by range of variability in MTTs) of the phantom was shown to be better than ±0.5 seconds in all cases. The peak enhancement measured in the ROIs was between 336 and 557 HU. The complete results of MTTs and peak enhancement for all measurement regions are shown in Table 1, with an example of the time-enhancement curves for 3 measurement regions shown in Figure 6.

DISCUSSION

The use of circulation phantoms in preclinical investigations has provided valuable insights that drove further understanding and optimization in the areas of contrast-enhanced CT over the past 2 decades. However, based on the aforementioned limitations of the second-generation design, the bounds of its preclinical utility are approaching. These drawbacks include limited arterial vascular models, a venous return comprised only of cylindrical silicone tubes, lack of an anatomical heart, a single-ventricle mechanical pump design allowing for only basic adjustment of heart rate and stroke volume while producing retrograde diastolic flow conditions, as well as a size and internal blood volume representing only a 40-kg human. In addition, the second-generation design effectively simulates only healthy human conditions, and although valuable as a stable model for comparing CM, injection systems, and differing protocols, it falls short

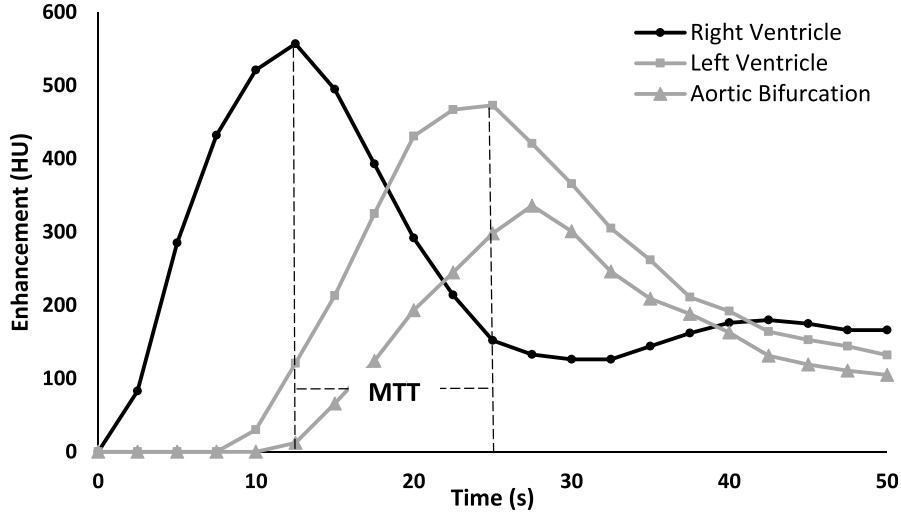

FIGURE 6. Time-enhancement curves for the right ventricle, left ventricle, and aortic bifurcation of the third-gen phantom, including example of MTT measurement.

of providing a platform for optimization of diagnosis and therapeutic intervention in cardiovascular disease states from head to toe.

As the field of CT continues to mature and advance (eg, continuation of drive toward lowest possible radiation exposure and iodinated CM administration), the necessity increases for a new robust preclinical testing platform, which allows for further investigation and optimization of techniques that translate to improvements in clinical practice. Furthermore, the concept of photon counting detector CT will offer new opportunities, especially in the field of cardiovascular disease.[9,33–35] The introduction of this third-gen phantom improves on the limitations of the second-generation design, including nearly complete venous and arterial vasculature, a 4-chamber heart model with embedded heart valves, modular design with models representing various disease states, an internal blood volume and size representing an average adult human, and improved control over cardiac function and physiological flow.

Based on the aforementioned history of the previous phantom generations, this represents a step forward in allowing for further optimization of radiation and contrast doses, comparatively assessing new imaging and injection techniques, and exploring areas of preclinical investigation. These include evaluation of cardiac disease, cerebral aneurysms, stents, calcified and soft arterial plaques, and many more that were previously either not investigated or evaluated in simple benchtop models. For example, evaluation of calcified plaques was previously conducted either in static phantoms or in static cadaver vessels filled with diluted CM or saline and placed in the gantry.[36,37] Although these types of evaluations provide directional information for researchers on impacts of varying scanner parameters, they miss the dynamic and transient aspects of the CM injection, circulatory blood flow, and cardiac motion. The ability of the third-gen phantom to use pressure and flow transducers to dial-in and validate the flow conditions, especially under pathologic conditions, will support future evaluations in this area. Without these confounders added to the equation, it is impossible to connect the dots for optimization of contrast injection and scan protocols. The use of the third-gen phantom allows for all of these variables to be put into play, and more importantly, to be varied independently for robust optimization. Figure 7 shows with CT images an injection of CM through the heart of the phantom, with nonhomogenous contrast and high attenuation within the right heart, and homogenous physiological attenuation in the left heart after the capacitive effect of the lung compartment. This demonstrates high translatability to in vivo clinical experience.

Of critical importance for a preclinical testing platform is the validation of its correlation to this in vivo expectation. The results herein provide reassurance that the dynamics of the third-gen phantom can simulate physiological flows and accurate CM transport and distribution dynamics of the human body. With accurate and repeatable transport timing, peak enhancement levels expected for CT angiography with these injection parameters,[17–24] and physiological dynamics inherently displayed through the time versus attenuation curves displayed herein, the third-gen phantom can be considered as a valuable precursor to clinical studies.

The MTTs between vascular landmarks for each of the 4 measurement regions were observed to be within the expected range based on values estimated from published literature. Contrast media arrival in the literature between antecubital vein and right ventricle was estimated between 10 and 16 seconds, with empirical phantom measurement of 13.1 ± 0.3 seconds.[17,18,38] Transit times from right ventricle to left ventricle were estimated from literature between 8 and 12 seconds, with phantom measurement of 12.0 ± 0.2 seconds.[17,18,38,39] From left ICA to left IJV, ranges estimated from literature were 7 to 10 seconds, whereas phantom measurements showed 7.7 ± 0.4 seconds.[40] Finally, transit times from aortic arch to aortic bifurcation were estimated from literature between 2.4 and 4 seconds and measured in the phantom at 2.9 ± 0.1 seconds.[17,18,41] The repeatability (measured by range of variability in MTTs) of the phantom was shown to be better than ±0.5 seconds in all cases, representing acceptable consistency considering the current temporal resolution of diagnostic imaging

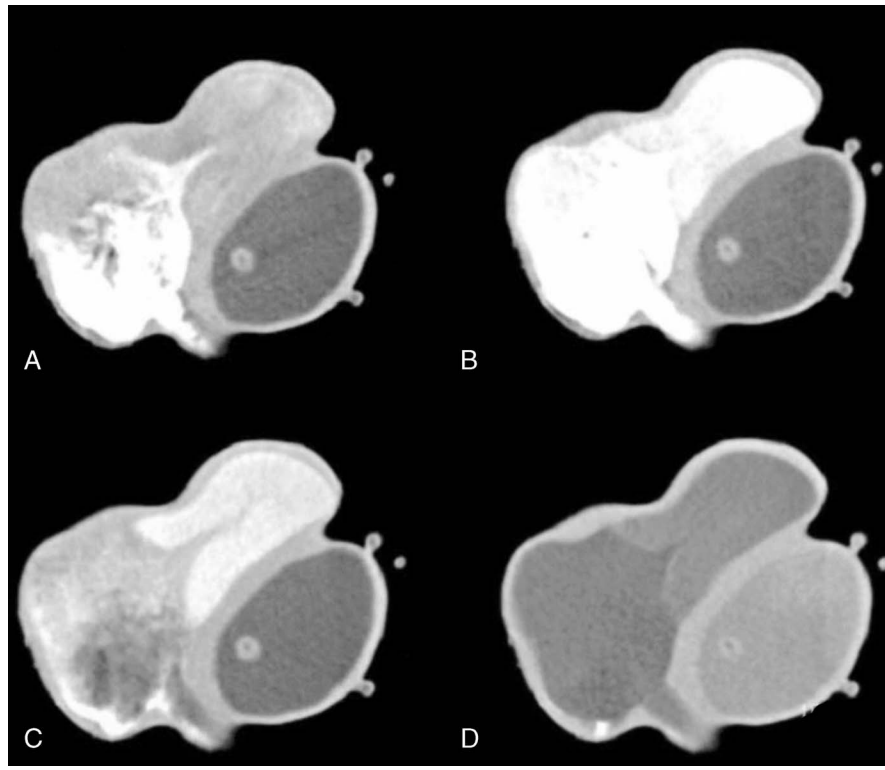

FIGURE 7. Computed tomography images of dynamic contrast material transport through the heart chambers, depicting nonhomogenously mixed contrast in the right ventricle (A and B), mixing action of the pulmonary valve (C), and more evenly distributed contrast material in the left heart upon pulmonary return (D).

equipment. The peak enhancement measured in the ROIs represents appropriate values, between 336 HU and 557 HU, based on the IDR (1.5 g I/s), internal blood volume (~5.5 L), and cardiac output of the phantom (5.3 L/min) when compared with accepted literature models.[16]

The third-gen phantom introduced is not simply confined to the CT suite, but rather as a complete dynamic circulatory model, it has potential implications across many different medical specialties. In addition to diagnostic imaging applications demonstrated, the complexity of the 4-chamber heart and diseased vascular models also potentially provides a stable and viable platform for training and evaluation of new procedures such as transcatheter aortic valve implantation, coronary stent deployment, aneurysm coiling and clipping, as well as plaque quantification and ultimately functional assessments.

Although the third-gen phantom opens up opportunities to the field of preclinical research, it does not yet represent the perfect model and does have its limitations. Primarily, the third-gen phantom does not include any soft tissue, organs, or attenuating structures outside of the blood vessels, therefore limiting its utility in parenchymal imaging. Although lacking this attenuating surrounding material and with an inability to simulate uptake of contrast medium by tissue and smaller structures, this is equivalent to previous circulation phantom generations in the study of first pass imaging, which did not limit their utility in previously published preclinical studies.

CONCLUSIONS

The introduction of the third-gen phantom provides a standardized physiological setup for preclinical research in diagnostic and interventional cardiovascular procedures. Based on a dynamic and controllable 4-chamber heart and the option for disease state simulations to be incorporated, this circulatory system model allows for the area of preclinical utility and translational application to clinical routine to be further expanded.

REFERENCES

1. Cormack AM. Early two-dimensional reconstruction (CT scanning) and recent topics stemming from it. *J Comput Assist Tomogr*. 1980;4:658–664.
2. Hounsfield GN. Computed medical imaging. Nobel lecture, December 8, 1979. *J Comput Assist Tomogr*. 1980;4:665–674.
3. Kalender WA, Seissler W, Klotz E, et al. Spiral volumetric CT with single-breath-hold technique, continuous transport, and continuous scanner rotation. *Radiology*. 1990;176:181–183.
4. Lell MM, Kachelrieß M. Recent and upcoming technological developments in computed tomography: high speed, low dose, deep learning, multienergy. *Invest Radiol*. 2020;55:8–19.
5. Wildberger JE, Prokop M. Hounsfield's legacy. *Invest Radiol*. 2020;55:556–558.
6. Willemink MJ, Noël PB. The evolution of image reconstruction for CT—from filtered back projection to artificial intelligence. *Eur Radiol*. 2019;29:2185–2195.
7. Schöckel L, Jost G, Seidensticker P, et al. Developments in x-ray contrast media and the potential impact on computed tomography. *Invest Radiol*. 2020;55:592–597.
8. Alkadhi H, Euler A. The future of computed tomography: personalized, functional, and precise. *Invest Radiol*. 2020;55:545–555.
9. Euler A, Higashigaito K, Mergen V, et al. High-pitch photon-counting detector computed tomography angiography of the aorta: intraindividual comparison to energy-integrating detector computed tomography at equal radiation dose. *Invest Radiol*. 2022;57:115–121.
10. Ginat DT, Gupta R. Advances in computed tomography imaging technology. *Annu Rev Biomed Eng*. 2014;16:431–453.
11. Stopsack KH, Cerhan JR. Cumulative doses of ionizing radiation from computed tomography: a population-based study. *Mayo Clin Proc*. 2019;94:2011–2021.
12. Yu JJ, Spieler BM, Chan TL, et al. Promoting collaborations between radiologists and scientists. *Acad Radiol*. 2018;25:9–17.
13. McDermott MC, Barone WR, Kemper CA. Proactive air management in CT power injections: a comprehensive approach to reducing air embolization. *IEEE Trans Biomed Eng*. 2021;68:1093–1103.
14. McDermott M, Kemper C, Barone W, et al. Impact of CT injector technology and contrast media viscosity on vascular enhancement: evaluation in a circulation phantom. *Br J Radiol*. 2020;93:20190868.
15. Overhoff D, Jost G, McDermott M, et al. Contrast saline mixture dualflow injection protocols for low-kilovolt computed tomography angiography: a systematic phantom and animal study. *Invest Radiol*. 2020;55:785–791.
16. Sahbaee P, Segars WP, Marin D, et al. The effect of contrast material on radiation dose at CT: part I. Incorporation of contrast material dynamics in anthropomorphic phantoms. *Radiology*. 2017;283:739–748.
17. Bae KT, Heiken JP, Brink JA. Aortic and hepatic contrast medium enhancement at CT. Part I. Prediction with a computer model. *Radiology*. 1998;207:647–655.
18. Bae KT, Heiken JP, Brink JA. Aortic and hepatic contrast medium enhancement at CT. Part II. Effect of reduced cardiac output in a porcine model. *Radiology*. 1998;207:657–662.
19. Awai K, Hatcho A, Nakayama Y, et al. Simulation of aortic peak enhancement on MDCT using a contrast material flow phantom: feasibility study. *Am J Roentgenol*. 2006;186:379–385.
20. Behrendt FF, Bruners P, Kalafut J, et al. Introduction of a dedicated circulation phantom for comprehensive in vitro analysis of intravascular contrast material application. *Invest Radiol*. 2008;43:729–736.
21. Kok M, Mihl C, Mingels AA, et al. Influence of contrast media viscosity and temperature on injection pressure in computed tomographic angiography: a phantom study. *Invest Radiol*. 2014;49:217–223.
22. De Santis D, Caruso D, Schoepf UJ, et al. Contrast media injection protocol optimization for dual-energy coronary CT angiography: results from a circulation phantom. *Eur Radiol*. 2018;28:3473–3481.
23. Kok M, Mihl C, Hendriks BM, et al. Optimizing contrast media application in coronary CT angiography at lower tube voltage: evaluation in a circulation phantom and sixty patients. *Eur J Radiol*. 2016;85:1068–1074.
24. Mihl C, Wildberger JE, Jurencak T, et al. Intravascular enhancement with identical iodine delivery rate using different iodine contrast media in a circulation phantom. *Invest Radiol*. 2013;48:813–818.
25. Bergel DH. The static elastic properties of the arterial wall. *J Physiol*. 1961;156:445–457.
26. Chaudhury RA, Atlasman V, Pathangey G, et al. A high performance pulsatile pump for aortic flow experiments in 3-dimensional models. *Cardiovasc Eng Technol*. 2016;7:148–158.
27. Ducci A, Tzamtzis S, Mullen MJ, et al. Hemodynamics in the Valsalva sinuses after transcatheter aortic valve implantation (TAVI). *J Heart Valve Dis*. 2013;22:688–696.
28. Cygan S, Werys K, Blaszczyk L, et al. Left ventricle phantom and experimental setup for MRI and echocardiography–preliminary results of data acquisitions. *Biocybernetics Biomed Engin*. 2014;34:19–24.
29. Mihl C, Kok M, Wildberger JE, et al. Computed tomography angiography with high flow rates: an in vitro and in vivo feasibility study. *Invest Radiol*. 2015;50:464–469.
30. Lell MM, Fleischmann U, Pietsch H, et al. Relationship between low tube voltage (70 kV) and the iodine delivery rate (IDR) in CT angiography: an experimental in-vivo study. *PLoS One*. 2017;12:e0173592.
31. Euler A, Taslimi T, Eberhard M, et al. Computed tomography angiography of the aorta—optimization of automatic tube voltage selection settings to reduce radiation dose or contrast medium in a prospective randomized trial. *Invest Radiol*. 2021;56:283–291.
32. American College of Radiology. 2022. Contrast Manual [online]. Available at: https://www.acr.org/Clinical-Resources/Contrast-Manual. Accessed July 18, 2021.
33. Boccalini S, Si-Mohamed SA, Lacombe H, et al. First in-human results of computed tomography angiography for coronary stent assessment with a spectral photon counting computed tomography. *Invest Radiol*. 2022;57:212–221.
34. Petritsch B, Petri N, Weng AM, et al. Photon-counting computed tomography for coronary stent imaging: in vitro evaluation of 28 coronary stents. *Invest Radiol*. 2021;56:653–660.
35. Allmendinger T, Nowak T, Flohr T, et al. Photon-counting detector CT-based vascular calcium removal algorithm: assessment using a cardiac motion phantom. *Invest Radiol*. 2022;57:399–405.
36. Sartoretti T, Eberhard M, Rüschoff JH, et al. Photon-counting CT with tungsten as contrast medium: experimental evidence of vessel lumen and plaque visualization. *Atherosclerosis*. 2020;310:11–16.
37. Sartoretti T, Eberhard M, Nowak T, et al. Photon-counting multienergy computed tomography with spectrally optimized contrast media for plaque removal and stenosis assessment. *Invest Radiol*. 2021;56:563–570.
38. Bae KT. Intravenous contrast medium administration and scan timing at CT: considerations and approaches. *Radiology*. 2010;256:32–61.
39. Seraphim A, Knott KD, Menacho K, et al. Prognostic value of pulmonary transit time and pulmonary blood volume estimation using myocardial perfusion CMR. *JACC Cardiovasc Imaging*. 2021;14:2107–2119.
40. Kuriyama Y, Aoyama T, Tada K, et al. Interrelationships among regional cerebral blood flow, mean transit time, vascular volume and cerebral vascular resistance. *Stroke*. 1974;5:719–724.
41. Akohov A, Barner C, Grimmer S, et al. Aortic volume determines global end-diastolic volume measured by transpulmonary thermodilution. *Intensive Care Med Exp*. 2020;8:1.